

TOWARD THE UNDERSTANDING OF THE PHYSICAL ORIGIN OF RECOMBINING PLASMA
IN THE SUPERNOVA REMNANT IC 443

HIDEAKI MATSUMURA,¹ TAKAAKI TANAKA,¹ HIROYUKI UCHIDA,¹ HIROMICHI OKON,¹ AND TAKESHI GO TSURU¹

¹*Department of Physics, Kyoto University, Kitashirakawa Oiwake-cho, Sakyo, Kyoto, Kyoto 606-8502, Japan*

(Accepted November 17, 2017)

ABSTRACT

We perform a spatially resolved spectroscopic analysis of X-ray emission from the supernova remnant (SNR) IC 443 with *Suzaku*. All the spectra are well reproduced by a model consisting of a collisional ionization equilibrium (CIE) and two recombining plasma (RP) components. Although previous X-ray studies found an RP in the northeastern region, this is the first report on RPs in the other parts of the remnant. The electron temperature kT_e of the CIE component is almost uniform at ~ 0.2 keV across the remnant. The CIE plasma has metal abundances consistent with solar and is concentrated toward the rim of the remnant, suggesting that it is of shocked interstellar medium origin. The two RP components have different kT_e : one in the range of 0.16–0.28 keV and the other in the range of 0.48–0.67 keV. The electron temperatures of both RP components decrease toward the southeast, where the SNR shock is known to be interacting with a molecular cloud. We also find the normalization ratio of the lower- kT_e RP to higher- kT_e RP components increases toward the southeast. Both results suggest the X-ray emitting plasma in the southeastern region is significantly cooled by some mechanism. One of the plausible cooling mechanisms is thermal conduction between the hot plasma and the molecular cloud. If the cooling proceeds faster than the recombination timescale of the plasma, the same mechanism can account for the recombining plasma as well.

Keywords: ISM: individual(IC 443), ISM: supernova remnants, X-rays: ISM, plasmas

arXiv:1711.06425v2 [astro-ph.HE] 20 Nov 2017

1. INTRODUCTION

IC 443 (G189.1+3.0) is a Galactic supernova remnant (SNR) at a distance of 1.5 kpc (Welsh & Sallmen 2003). Its age is estimated to be in the range of 3–30 kyr (Petre et al. 1988; Olbert et al. 2001). Olbert et al. (2001) found a pulsar wind nebula (PWN) in the southeastern part of the remnant, suggesting that IC 443 is a remnant of a core-collapse supernova. Seen in the radio and optical bands, IC 443 has two shells with different radii (e.g., Lee et al. 2008). The remnant is categorized as a mixed-morphology SNR (Rho & Petre 1998) since the X-ray emission has a center-filled morphology.

In X-rays, Kawasaki et al. (2002) measured the $\text{Ly}\alpha$ to $\text{He}\alpha$ line intensity ratio of Si and S with *ASCA*, and found that the plasma in the northeastern part of the remnant is more ionized than expected in collisional ionization equilibrium (CIE). With *Suzaku*, Yamaguchi et al. (2009) discovered radiative recombining continua (RRCs) of Si and S in the northeastern region, which provided unambiguous evidence for a recombining plasma (RP). Ohnishi et al. (2014) found RRCs of Ca and Fe in almost the same region as Yamaguchi et al. (2009) and indicated that heavier elements are also overionized.

The formation process of RPs, now observed also in other Galactic and Large Magellanic Cloud SNRs (e.g., Ozawa et al. 2009; Uchida et al. 2015), has not been fully understood yet and is still under debate. The rarefaction scenario (Itoh & Masai 1989) and the thermal conduction scenario (Kawasaki et al. 2002) are mainly discussed in the literature. Itoh & Masai (1989) proposed that RPs are realized by adiabatic cooling when the SNR shock breaks out of a dense circumstellar matter into a lower density interstellar medium (ISM). Kawasaki et al. (2002) suggested that the electron temperature (kT_e) of the plasma is lowered by thermal conduction between the SNR plasma and a molecular cloud interacting with the SNR. With *Suzaku* observations of the SNR G166.0+4.3, Matsumura et al. (2017) found an RP only in a part of the remnant with higher ambient gas density, which favors the thermal conduction scenario. On the other hand, with *Chandra* observations of W49B, Lopez et al. (2013) found that the plasma has a gradient of kT_e increasing toward a region where higher density ISM is present. They claimed that the dominant cooling mechanism is adiabatic expansion of the hot plasma.

IC 443 is interacting with both molecular and atomic gas (e.g., Lee et al. 2008). Cornett et al. (1977) discovered a dense molecular cloud associated with IC 443. CO line emissions in the southeastern part of the remnant suggest that the molecular cloud is interacting with IC 443 (e.g., Denoyer 1979; Xu et al. 2011; Yoshiike 2017). Measurements of the CO line velocity by Yoshiike (2017) suggest that the most part of the interacting molecular gas is located in front of

IC 443. In the northeast, the SNR shock emits atomic lines expected from post-shock recombining gas (Fesen & Kirshner 1980), and therefore, the shock is likely to be propagating into an atomic medium. Near-infrared observations also support the atomic gas in the northeast (e.g., Kokusho et al. 2013).

In this paper, we perform spatially resolved X-ray spectroscopy of the SNR IC 443 with *Suzaku* and compare the results with the distribution of interstellar gas interacting with the remnant. We then discuss the implications particularly on the formation process of the RP. Throughout the paper, errors are quoted at 90% confidence levels in the text and tables, and error bars in the figures indicate 1σ confidence intervals. All spectral fits are performed with XSPEC version 12.9.0n. The plasma models are calculated with ATOMDB version 3.0.8. We used solar abundances given by Wilms et al. (2000).

2. OBSERVATIONS AND DATA REDUCTION

Table 1 summarizes the *Suzaku* observation log of IC 443. We used the data from the X-ray Imaging Spectrometer (XIS; Koyama et al. 2007), which consists of four X-ray CCD cameras installed on the focal planes of the X-Ray Telescopes (XRT; Serlemitsos et al. 2007). XIS0, 2 and 3 have front-illuminated sensors whereas XIS1 has a back-illuminated one. XIS2 and a part of XIS0 have not been functioning since November 2006 and June 2009, respectively (*Suzaku* XIS documents^{1,2}). Therefore, we do not use XIS2 and the part of XIS0 for the data acquired after those times.

We reduced the data using the HEADAS software version 6.19. We used the calibration database released in April 2016 for processing the data. We removed flickering pixels by referring to the noisy pixel maps³ provided by the XIS team. We also discarded pixels adjacent to the flickering pixels. Non X-ray backgrounds (NXBs) were estimated by `xisnxbgen` (Tawa et al. 2008). Redistribution matrix files and ancillary response files were produced by `xisrmfgen` and `xissimarfgen` (Ishisaki et al. 2007), respectively.

Analyzing the XIS0 and 3 data taken in 2007, we noticed that the centroid energies of $\text{Ly}\alpha$ lines from IC 443, and Mn $\text{K}\alpha$ and $\text{K}\beta$ lines from the on-board calibration sources are shifted by 2–8 eV from the true values. Although this is well within the calibration uncertainties, < 20 eV at Mn $\text{K}\alpha$, reported by the XIS team⁴, residuals caused by the gain shift are not negligible with the high statistics of the present data. Those artificial residuals sometimes make it

¹ <http://www.astro.isas.ac.jp/suzaku/doc/suzakumemo/suzakumemo-2007-08.pdf>

² <http://www.astro.isas.ac.jp/suzaku/doc/suzakumemo/suzakumemo-2010-01.pdf>

³ <https://heasarc.gsfc.nasa.gov/docs/suzaku/analysis/xisnxbnew.html>

⁴ https://heasarc.gsfc.nasa.gov/docs/suzaku/prop_tools/suzaku_td/

difficult to clearly see important residuals in the spectral fitting described in §3. We, therefore, corrected the gain of the XIS0 and 3 data from each observation. We fitted narrow-band spectra in each energy band around the O VIII, Mg XII, Si XIV, and S XVI lines from IC 443, and Mn $K\alpha$ and $K\beta$ lines from the calibration sources with a Gaussian and a power law for the underlying continuum. We here did not use the Ne X line because it overlaps with the Fe-L line complex. We then fitted the relation between the true energies and the centroid energies of the Gaussians with a first-order polynomial. We corrected the gain using the polynomial function.

3. ANALYSIS

3.1. Image

Figure 1a shows an XIS3 image of IC 443 in the energy band of 0.3–2.0 keV. We subtracted the NXB from the image and corrected for the vignetting effect of the XRT. The X-ray emissions in the east are center-filled as is previously known (e.g., Troja et al. 2006). In the northwest, the image shows a hint of a shell-like structure.

Figure 1b shows an XIS3 image in the 3.0–5.0 keV band. We found the PWN 1SAX J0617.1+2221 (region A) and the point source U061530.75+224910.6 (region B) (Bocchino & Bykov 2001, 2003). We found two additional point sources in the northwest and a source in the northeast which are already detected in *XMM-Newton* data by Bocchino & Bykov (2003). We excluded the PWN and the point sources for our spectral analysis of IC 443.

3.2. X-ray Background Estimation

We used *Suzaku* data of IRAS 05262+4432, which is located at (R.A., Dec.) = ($5^{\text{h}}29^{\text{m}}56^{\text{s}}.0$, $44^{\circ}34'39''.2$), for background estimation. The observation log is shown in Table 1. We extracted a spectrum from a source-free region and fitted it with a model by Masui et al. (2009), who studied the soft X-ray emission from the anti-center region of the Galaxy with *Suzaku*. The model consists of four components: the cosmic X-ray background (CXB), the local hot bubble (LHB), and two thermal components for the Galactic halo (GH_{cold} and GH_{hot}). We used the Wisconsin absorption model (Wabs; Morrison & McCammon 1983) for the absorption column density (N_{H}) and fixed it at $3.8 \times 10^{21} \text{ cm}^{-2}$, which is the total Galactic absorption in the line of sight toward IRAS 05262+4432 (Dickey & Lockman 1990). We fixed the photon index of the CXB component and kT_e of the LHB, GH_{cold} and GH_{hot} components at the values given by Masui et al. (2009). The best-fit parameters are shown in Table 2. We used this model as the background spectrum for IC 443 in subsection 3.3 but with N_{H} of the CXB component changed to $6.1 \times 10^{21} \text{ cm}^{-2}$, which corresponds to the total Galactic absorption in the line of sight toward IC 443.

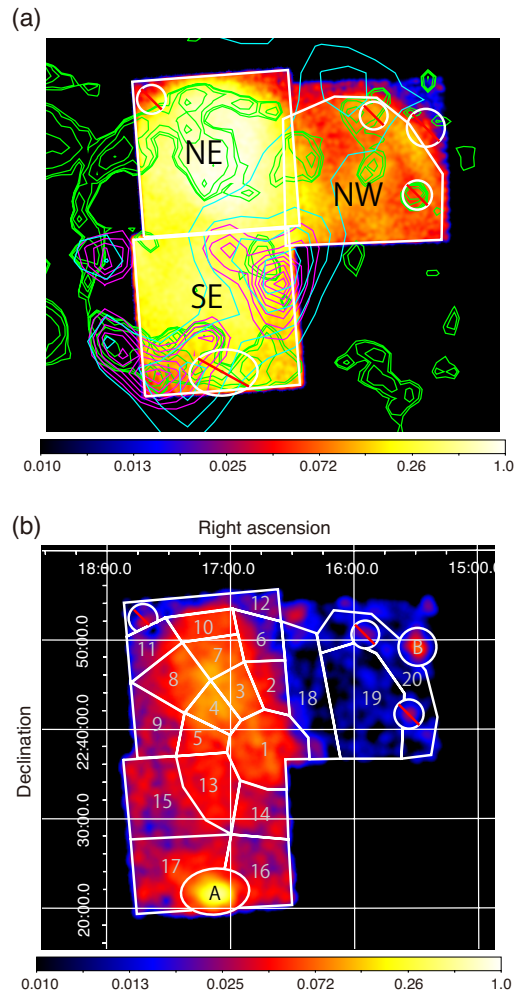


Figure 1. XIS3 images of IC 443 in the energy band of (a) 0.3–2.0 keV and (b) 3.0–5.0 keV after NXB subtraction and correction of the vignetting effect. In panel (a), we overlaid green contours of 1.4 GHz radio image which were obtained from the NRAO VLA Sky Survey (NVSS). The cyan and magenta contours are radio images of $^{12}\text{CO}(J=1-0)$ and $^{12}\text{CO}(J=2-1)$ obtained from the NAN-TEN2, respectively (Yoshiike 2017). Sources in regions A and B in panel (b) are the PWN 1SAX J0617.1+2221 and the point source U061530.75+224910.6, respectively. The X-ray count rates is normalized so that the peak becomes unity. The coordinate refers to the J2000.0 epoch.

3.3. SNR spectra

Previous X-ray studies found that the spectra in the northeastern region can be reproduced with RP models (Yamaguchi et al. 2009; Ohnishi et al. 2014). In order to examine ionization states of the SNR plasmas in the other regions, we extracted spectra from the southeast (SE), northwest (NW) and northeast (NE) regions shown in Figure 1a.

Figure 2 shows the XIS0+3 spectrum of the SE region after NXB subtraction. The characteristic structures of Si

Table 1. Observation log.

Target	Obs. ID	Obs. date	(R.A., Dec.)	Effective Exposure
IC 443 northeast	501006010	2007-03-06	(6 ^h 17 ^m 11 ^s .4, 22°46′32″.5)	42 ks
IC 443 southeast	501006020	2007-03-07	(6 ^h 17 ^m 11 ^s .3, 22°28′46″.9)	44 ks
IC 443 northwest	505001010	2010-09-17	(6 ^h 15 ^m 59 ^s .4, 22°45′18″.7)	83 ks
IRAS 05262+4432 (Background)	703019010	2008-09-14	(5 ^h 29 ^m 56 ^s .0, 44°34′39″.2)	82 ks

Table 2. Best-fit model parameters for the background.

Component	Model function	Parameter	Value
CXB	Wabs	N_{H} (10^{22} cm ⁻²)	0.38 (fixed)
	Power law	Photon index	1.4 (fixed)
		Normalization*	10.7 ± 0.4
LHB	APEC	kT_e (keV)	0.105 (fixed)
		Normalization [†]	13.4 ± 3.2
GH _{cold}	APEC	kT_e (keV)	0.658 (fixed)
		Normalization [†]	2.1 ± 0.2
GH _{hot}	APEC	kT_e (keV)	1.50 (fixed)
		Normalization [†]	3.1 ± 0.5
		χ^2_{ν} (ν)	1.29 (234)

NOTE—*The unit is photons s⁻¹ cm⁻² keV⁻¹ sr⁻¹ at 1 keV.

[†]The emission measure integrated over the line of sight, i.e., $(1/4\pi) \int n_e n_{\text{H}} dl$ in units of 10^{14} cm⁻⁵ sr⁻¹.

and S RRCs indicate that the plasma is in a recombination-dominant state. Following Yamaguchi et al. (2009), we first analyzed the spectrum in the energy band above 1.6 keV in order to quantify the ionization states of Si and S. We applied a model consisting of one RP component to the spectrum. We used the VVRNEI model in XSPEC, which calculates the spectrum of a non-equilibrium ionization plasma after a rapid transition of the electron temperature from kT_{init} to kT_e . The initial plasma temperature kT_{init} was fixed at 5 keV, in which most Si and S ions become bare nuclei. The present electron temperature kT_e and ionization parameter $n_e t$ were allowed to vary. The abundances of Si, S, Ar, Ca and Fe were allowed to vary, whereas the Ni abundance was linked to Fe. The abundances of the other elements were fixed to solar. We used the Tuebingen-Boulder ISM absorption model (TBabs; Wilms et al. 2000), whose column density was fixed at 7.0×10^{21} cm⁻² as determined by Kawasaki et al. (2002). For the XIS0+3 spectrum, we ignored the energy band of 1.78–1.92 keV be-

cause of the known calibration uncertainty around the neutral Si K-edge. Although we excluded the PWN from the spectrum extraction region, there is non-negligible leakage from the PWN due to the tail of the point spread function of the XRT. We, therefore, added a power law to account for the PWN emission. We fixed the photon index at 1.89 given by our spectral analysis of the PWN region (see Appendix A).

Figure 3a and Table 3 show the fitting results and the best-fit parameters, respectively. The spectrum is reproduced well by the model with $kT_e = 0.30 \pm 0.01$ keV and $n_e t = (4.6 \pm 0.1) \times 10^{11}$ s cm⁻³. The electron temperature is significantly smaller than $0.61^{+0.03}_{-0.02}$ keV given by Yamaguchi et al. (2009). They fitted the spectrum with a phenomenological model consisting of a CIE component, Gaussians for Si, S and Ar Ly α lines and RRCs of Mg, Si and S. We here used a more physically oriented model that takes into account ion fractions and ionization timescales of all elements in the recombination-dominant state. In this model, RRCs of Ne and of lighter elements, which are not included in the model employed by Yamaguchi et al. (2009), extend up to the Si–S band. This difference would be the reason why we obtained lower kT_e .

We extrapolated the above model down to 0.6 keV, which results in large residuals in the soft band. We added a CIE component to the model following Kawasaki et al. (2002) and Bocchino et al. (2009), who modeled IC 443 spectra with two-component models with a CIE component for the soft band. The result is shown in Figure 3b and Table 3. Since we found the abundances of the CIE component are close to solar, we fixed them at solar values. The fit left residuals around 1.23 keV, most probably due to the lack of Fe-L lines in the model (e.g., Yamaguchi et al. 2011), and therefore, we added a Gaussian at 1.23 keV. The fit still left residuals at 0.87 keV, indicating a shortage of the emission line of Fe XVIII 1s2 2s2 2p4 3d1 \rightarrow 1s2 2s2 2p5. To make the line stronger with $n_e t \sim 10^{11}$ s cm⁻³, kT_e is required to be higher than ~ 0.5 keV.

We then fitted the spectrum with a model consisting of a power-law, a CIE, an RP and an additional higher kT_e components. We tried CIE, ionizing plasma (IP), and RP models as the high kT_e component, and found that the CIE and IP models fail to fit the spectrum. We applied a model consisting of

a CIE and two RP components to the spectrum. The spectrum is well reproduced by the model with the significantly different kT_e between the two RP components whereas $n_e t$ and abundances of the two components are almost the same. Therefore, we linked $n_e t$ and the abundances of the components to each other. The best-fit model and parameters are shown in Figure 3c and Table 3, respectively. The residuals at the Fe XVIII line was significantly improved. The electron temperatures of the CIE and two RP (named RP_{cold} and RP_{hot}) components are 0.22 ± 0.01 keV, 0.19 ± 0.01 keV and $0.54^{+0.03}_{-0.01}$ keV, respectively. The ionization timescale of the RP components is $n_e t = (4.2^{+0.2}_{-0.1}) \times 10^{11}$ s cm⁻³.

We performed spectral fitting of the NW and NE spectra in the same procedure as we did for the SE spectrum. We found that the model consisting of a CIE and two-RP components gives satisfactory fits to both spectra. The spectra with the best-fit models are plotted in Figures 4a and 4b and the best-fit parameters are again summarized in Table 3. The ionization parameter $n_e t$ of the NW spectrum is close to 2×10^{12} s cm⁻³, which is a characteristic timescale for a plasma to reach CIE (Masai 1994). Therefore, the RP in the NW is close to CIE. Since we cannot fit the spectrum in the energy band of the Fe-L complex of the NW spectrum, we allowed the Fe abundance of the CIE component to vary. The fit gave somewhat higher Fe abundance of 1.3 ± 0.1 , but the abundance is still close to solar. Although kT_e and $n_e t$ of the NW and NE spectra are close to those of the SE spectrum, normalization ratios of the RP components are significantly different, indicating that the RP components have spatial variation.

In order to conduct spatially resolved spectroscopy in greater detail, we divided the remnant into 20 regions as shown in Figure 1b and extracted spectra from each region. We fitted the spectra with the above model, and found that it reproduces all the spectra well. The details of the fits are described in Appendix B. Since the leakage from the PWN and the point sources contaminate the spectra of regions 16, 17 and 20, we added a power law to the model for these spectra. The photon indices were fixed at 1.89 and 2.22, which are determined by our analysis in Appendix A, for the PWN and the point-source U061530.75+224910.6, respectively. The obtained ranges of kT_e are 0.19–0.28 keV, 0.16–0.28 keV and 0.48–0.67 keV for the CIE, RP_{cold} and RP_{hot} components, respectively. The electron temperature of the CIE component is uniform whereas those of the RP_{cold} and RP_{hot} components decrease toward the southeast as shown in Figure 5. Figures 6a and 6b show the map of N_H and $n_e t$, respectively. In the northwest, $n_e t$ is larger than those of the other regions.

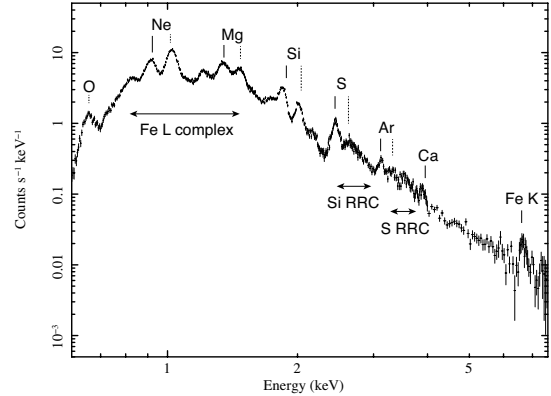


Figure 2. XIS0+3 spectrum of the SE region after NXB subtraction. The vertical solid and dashed black lines indicate the centroid-energies of He α and Ly α lines, respectively. The arrows indicate the energy bands of the Fe-L complex and the radiative recombining continua of Si and S.

4. DISCUSSION

4.1. Absorption by the Molecular Cloud

Figure 6a shows the spatial distribution of the X-ray absorption column densities (hereafter $N_{H,X}$). Since our analysis covers almost the whole remnant, we can perform a systematic comparison between $N_{H,X}$ and the ambient gas distribution. Our spectral fits gave high $N_{H,X}$ in regions 1, 2, 5, 6, 13, 14, 16, 17 and 18, which coincide with the locations of the molecular cloud traced by the ¹²CO($J = 1-0$) line (e.g., Xu et al. 2011; Yoshiike 2017). Our result indicates that the cloud is located in front of the remnant. If we subtract the lowest $N_{H,X}$ (region 19) from the highest one (region 14), we obtain $(3.1 \pm 0.6) \times 10^{21}$ cm⁻², which can be attributed to the absorption by the molecular cloud.

Yoshiike (2017) observed the ¹²CO($J = 1-0$) line with the NANTEN2 telescope, and concluded that the molecular cloud is located in front of IC 443 based on line velocity measurements. We note that Troja et al. (2006) also reached the same conclusion based on a comparison between *XMM-Newton* data and CO data. Yoshiike (2017) estimated the column density of the molecular cloud to be $N_{H,CO} = (6.1 \pm 0.8) \times 10^{21}$ cm⁻². Although the estimate by Yoshiike (2017) is somewhat larger than ours, the two measurements can be regarded to be consistent with each other, considering the fact that the estimate by Yoshiike (2017) is obtained for the CO emission peak location and that our estimate is an average of a much larger region.

4.2. Origin of the CIE plasma

In the spectral analysis, we successfully reproduced the spectra from all the regions with the model consisting of the CIE, RP_{cold} and RP_{hot} components. The abundances of the

Table 3. Best-fit model parameters of the SE, NW and NE spectra.

Model function	Parameter	SE	SE	SE	NW	NE
		1.6–7.5 keV	0.6–7.5 keV	0.6–7.5 keV	0.6–7.5 keV	0.6–7.5 keV
TBabs	N_{H} (10^{22} cm $^{-2}$)	0.70 (fixed)	0.90 $^{+0.02}_{-0.01}$	0.88 $^{+0.01}_{-0.02}$	0.74 $^{+0.02}_{-0.03}$	0.85 $^{+0.01}_{-0.01}$
VVRNEI1	kT_e (keV)	————	0.28 $^{+0.01}_{-0.03}$	0.22 $^{+0.01}_{-0.01}$	0.26 $^{+0.02}_{-0.02}$	0.23 $^{+0.01}_{-0.01}$
(CIE comp.)	$Z_{\text{Fe}} = Z_{\text{Ni}}$ (solar)	————	1 (fixed)	1 (fixed)	1 (fixed)	1.3 $^{+0.1}_{-0.1}$
	Z_{other} (solar)	————	1 (fixed)	1 (fixed)	1 (fixed)	1 (fixed)
	VEM (10^{57} cm $^{-3}$) †	————	8.9 $^{+2.1}_{-0.6}$	14.2 $^{+1.6}_{-1.9}$	3.5 $^{+1.3}_{-1.0}$	35.1 $^{+2.2}_{-3.9}$
VVRNEI2	kT_e (keV)	0.30 $^{+0.01}_{-0.01}$	0.26 $^{+0.01}_{-0.01}$	0.19 $^{+0.01}_{-0.01}$	0.22 $^{+0.06}_{-0.01}$	0.24 $^{+0.01}_{-0.01}$
(RP $_{\text{cold}}$ comp.)	kT_{init} (keV)	5 (fixed)				
	Z_{O} (solar)	1 (fixed)	1 (fixed)	1 (fixed)	1 (fixed)	2.4 $^{+0.6}_{-0.3}$
	Z_{Ne} (solar)	1 (fixed)	2.4 $^{+0.2}_{-0.1}$	3.2 $^{+0.2}_{-0.2}$	1.5 $^{+0.2}_{-0.2}$	3.8 $^{+0.4}_{-0.3}$
	Z_{Mg} (solar)	1 (fixed)	1.5 $^{+0.1}_{-0.1}$	1.6 $^{+0.1}_{-0.1}$	1.1 $^{+0.1}_{-0.1}$	2.2 $^{+0.3}_{-0.1}$
	Z_{Si} (solar)	1.1 $^{+0.1}_{-0.1}$	1.5 $^{+0.1}_{-0.1}$	1.8 $^{+0.1}_{-0.1}$	0.8 $^{+0.1}_{-0.1}$	3.9 $^{+0.4}_{-0.2}$
	Z_{S} (solar)	0.6 $^{+0.1}_{-0.1}$	0.9 $^{+0.1}_{-0.1}$	1.2 $^{+0.1}_{-0.1}$	0.5 $^{+0.1}_{-0.1}$	2.6 $^{+0.4}_{-0.1}$
	Z_{Ar} (solar)	0.6 $^{+0.1}_{-0.1}$	0.8 $^{+0.1}_{-0.1}$	1.2 $^{+0.1}_{-0.1}$	= Z_{S}	2.4 $^{+0.2}_{-0.2}$
	Z_{Ca} (solar)	0.6 $^{+0.1}_{-0.1}$	0.8 $^{+0.2}_{-0.1}$	1.2 $^{+0.2}_{-0.2}$	= Z_{S}	2.2 $^{+0.3}_{-0.2}$
	$Z_{\text{Fe}} = Z_{\text{Ni}}$ (solar)	0.2 $^{+0.1}_{-0.1}$	0.1 $^{+0.1}_{-0.1}$	0.5 $^{+0.1}_{-0.1}$	0.2 $^{+0.1}_{-0.1}$	0.8 $^{+0.1}_{-0.1}$
	$n_e t$ (10^{11} s cm $^{-3}$)	4.6 $^{+0.1}_{-0.1}$	4.1 $^{+0.2}_{-0.1}$	4.2 $^{+0.2}_{-0.1}$	9.7 $^{+0.9}_{-1.1}$	5.4 $^{+0.1}_{-0.1}$
	VEM (10^{57} cm $^{-3}$) †	30.5 $^{+1.4}_{-1.4}$	21.7 $^{+0.5}_{-0.9}$	12.6 $^{+0.7}_{-1.0}$	2.4 $^{+0.8}_{-1.4}$	7.0 $^{+0.4}_{-0.5}$
VVRNEI3	kT_e (keV)	————	————	0.54 $^{+0.03}_{-0.01}$	0.63 $^{+0.02}_{-0.01}$	0.61 $^{+0.01}_{-0.01}$
(RP $_{\text{hot}}$ comp.)	kT_{init} (keV)	————	————	5 (fixed)	5 (fixed)	5 (fixed)
	Z_{all} (solar)	————	————	= RP $_{\text{cold}}$	= RP $_{\text{cold}}$	= RP $_{\text{cold}}$
	$n_e t$ (10^{11} s cm $^{-3}$)	————	————	= RP $_{\text{cold}}$	= RP $_{\text{cold}}$	= RP $_{\text{cold}}$
	VEM (10^{57} cm $^{-3}$) †	————	————	4.1 $^{+0.2}_{-0.4}$	1.8 $^{+0.1}_{-0.2}$	6.8 $^{+0.4}_{-0.9}$
Gaussian	Centroid (keV)	————	1.23 (fixed)	1.23 (fixed)	1.23 (fixed)	1.23 (fixed)
	Normalization ‡	————	132 $^{+15}_{-15}$	56 $^{+8}_{-9}$	49 $^{+16}_{-6}$	142 $^{+18}_{-19}$
Power law	Photon index	1.89 (fixed)	1.89 (fixed)	1.89 (fixed)	————	————
	Normalization*	151 $^{+23}_{-23}$	171 $^{+22}_{-20}$	130 $^{+12}_{-14}$	————	————
	χ^2_{ν} (ν)	1.55 (594)	1.71 (1126)	1.47 (1124)	1.23 (838)	1.67 (1123)

NOTE— † Volume emission measure at the distance of 1.5 kpc: $VEM = \int n_e n_{\text{H}} dV$, where n_e , n_{H} , and V are the electron and hydrogen densities, and the emitting volume, respectively.

‡ The unit is photons s $^{-1}$ cm $^{-2}$ sr $^{-1}$. *The unit is photons s $^{-1}$ cm $^{-2}$ keV $^{-1}$ sr $^{-1}$ at 1 keV.

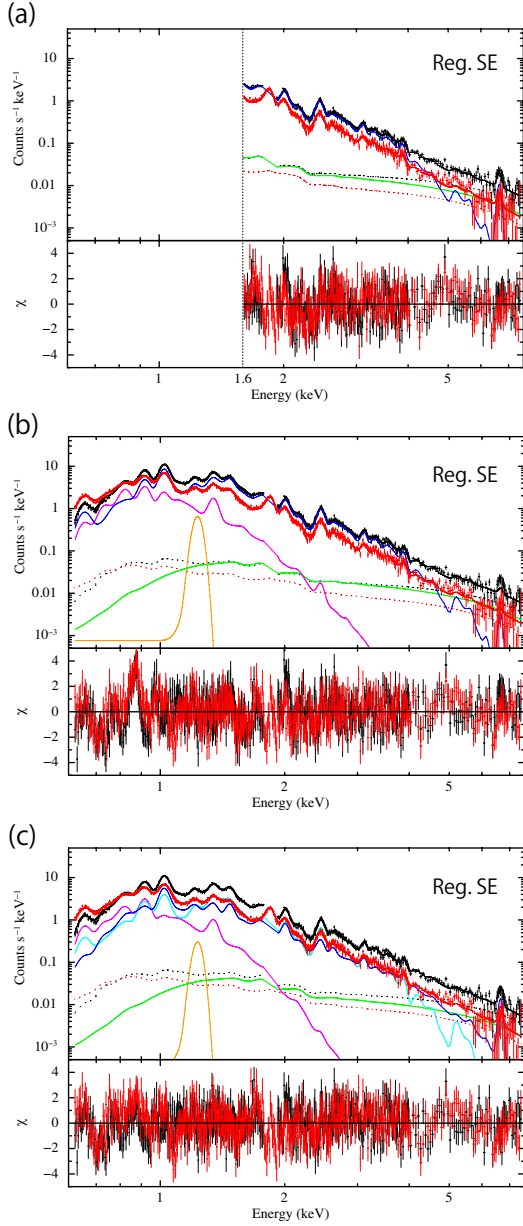


Figure 3. XIS0+3 (black crosses) and XIS1 (red crosses) spectra in the SE region. Each spectrum is fitted with the model consisting of the SNR and background components. The magenta, cyan, blue, green, and orange solid lines show the SNR models for XIS0+3, consisting of CIE, RP_{cold} , RP_{hot} , power-law, Gaussian components, respectively. The black and red dotted lines denote the background model for the XIS0+3 and XIS1 spectra, respectively. The sum of the SNR and background models for XIS0+3 and XIS1 are shown by the black and red solid lines, respectively.

CIE component are consistent with solar, suggesting that the component is of shocked ISM origin. The spatial distribution of the component also supports this picture. Figure 7a-1 shows the normalization ratios of the CIE component to the

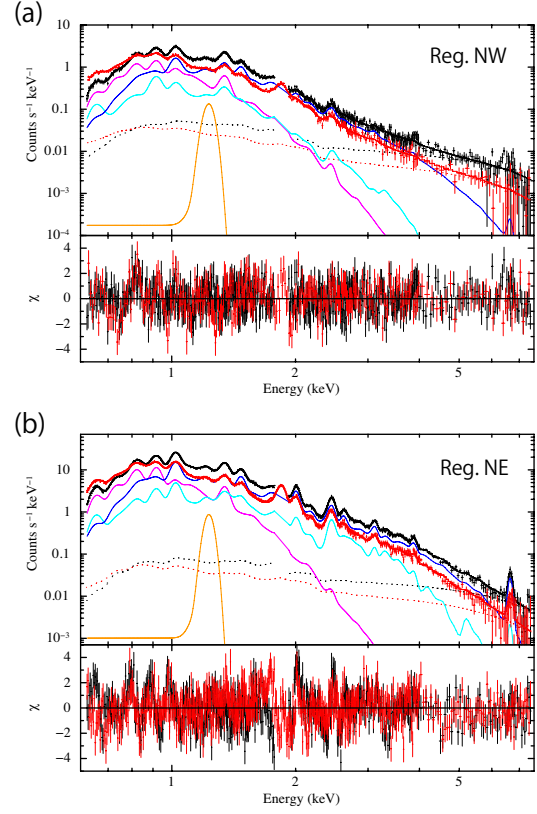


Figure 4. Same as Figure 3 but for the (a) NW and (b) NE spectra.

RP_{hot} component plotted as a function of the angular distance from the center of the remnant which we define as (R.A., Dec.) = ($6^{\text{h}}16^{\text{m}}40^{\text{s}}.0$, $22^{\circ}38'00''.0$). The map of the normalization ratio is shown in Figure 7a-2. The normalization ratios tend to increase toward the outer regions, suggesting that the CIE plasma is concentrated in the rim as is generally expected for a shocked ISM emission.

4.3. Origin of the recombining plasmas

In section 3.3, we found that the emission is well reproduced by a model which includes two RP components with different kT_e . As shown in Figure 5, the electron temperatures of both components decrease toward the southeast. The southeastern region coincides with the locations where the molecular cloud is known to be interacting with the remnant based on the $^{12}\text{CO}(J=2-1)$ to $^{12}\text{CO}(J=1-0)$ intensity ratio (e.g., Xu et al. 2011; Yoshiike 2017). The normalization ratio of the two RP components points to a similar tendency. Figures 7b-1 and 7b-2 show a radial profile and a map of the RP_{cold} to RP_{hot} normalization ratio, respectively. As opposed to Figure 7a-1, no clear correlation is seen in the radial profile. From the map, it is evident that the ratio is larger in the southeastern region, where kT_e is also lower than the other regions (see Figure 5). These results on kT_e and the normal-

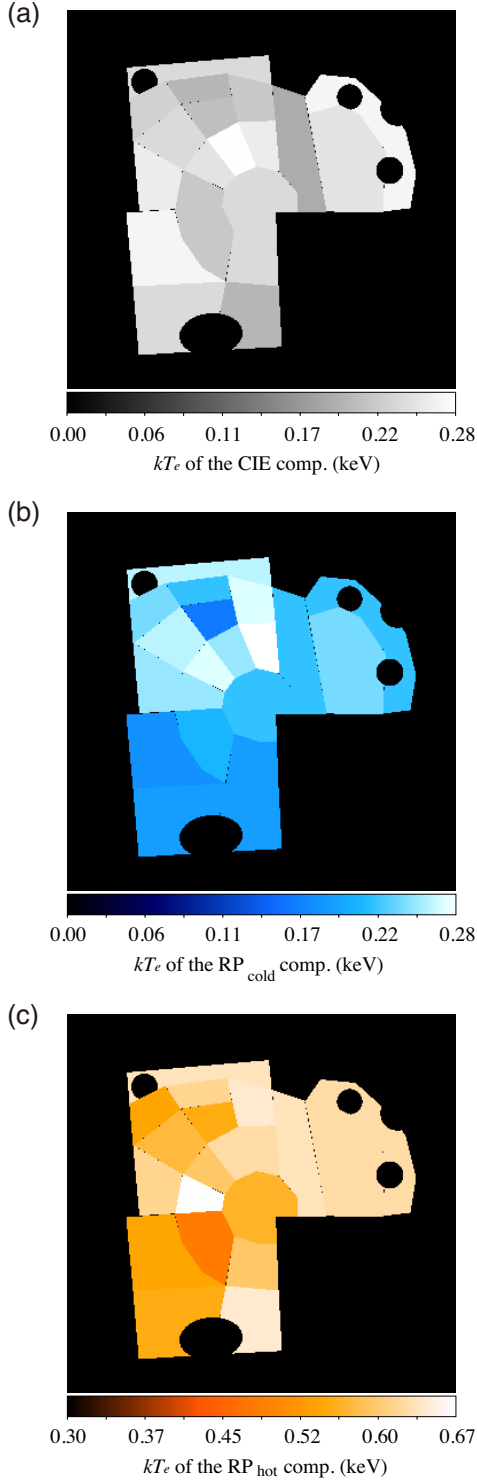


Figure 5. Maps of the electron temperatures kT_e of the (a) CIE, (b) RP_{cold} , (c) RP_{hot} components.

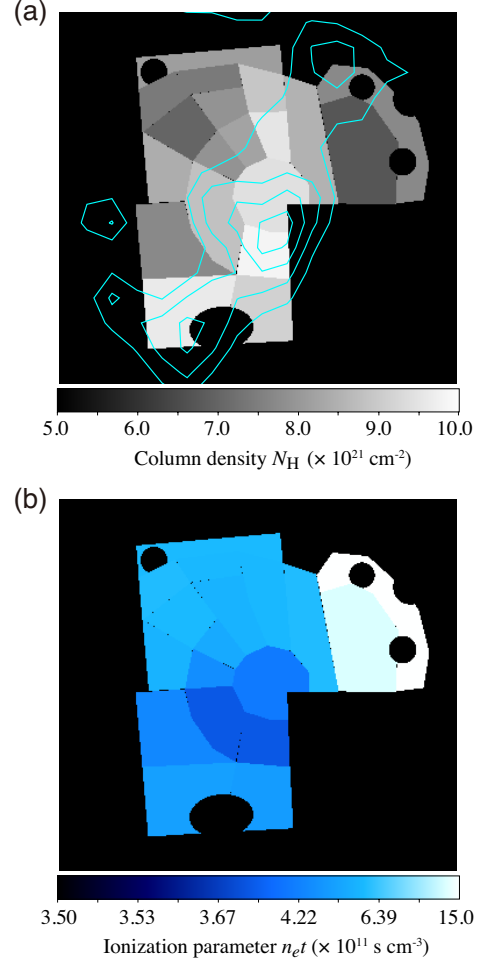


Figure 6. (a) Map of the column density N_{H} with the $^{12}\text{CO}(J=1-0)$ emissions (cyan contours; Yoshiike 2017). (b) Map of the ionization parameters $n_e t$.

ization ratio together indicate that the SNR plasma is cooler in the region where the shock is in contact with the molecular cloud.

One of the plausible mechanisms to explain the cooler plasma in the southeastern region is cooling of the X-ray emitting plasma by the molecular cloud via thermal conduction. If the cooling proceeds faster than the recombination timescale of the plasma, the recombining plasma can also be explained by the thermal conduction. In this scenario, continuous cooling until the present day may have resulted in the smallest $n_e t$ in the southeast (Figure 6b). The thermal conduction scenario is proposed for the formation process of an RP in G166.0+4.3 by Matsumura et al. (2017), who found kT_e of a high-density region of the SNR is significantly lower than that of a low-density region. Their observational result is in fact similar to our findings on IC 443 reported in this paper. On the contrary, as discussed by Lopez et al. (2013)

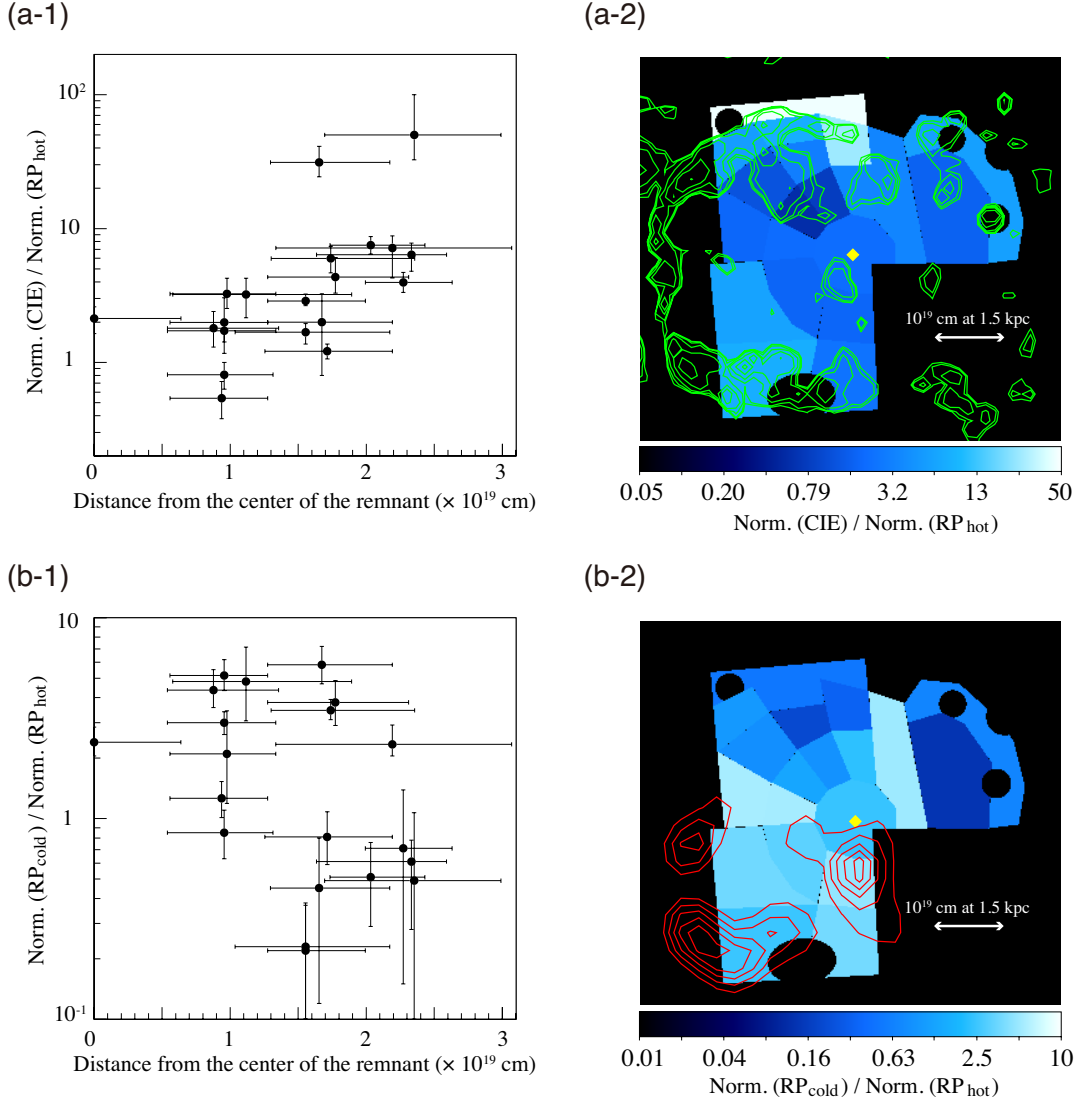


Figure 7. (a-1) Radial profile and (a-2) map of the CIE to RP_{hot} normalization ratio with the 1.4 GHz radio emissions (green contours). (b-1) Radial profile and (b-2) map of the RP_{cold} to RP_{hot} normalization ratio with a map of the $^{12}\text{CO}(J=2-1)$ to $^{12}\text{CO}(J=1-0)$ intensity ratio (red contours; Yoshiike 2017). The yellow diamonds denote the center of the remnant (R.A., Dec.) = ($6^{\text{h}}16^{\text{m}}40^{\text{s}}0$, $22^{\circ}38'00''0$). The length of the white arrows correspond to 10^{19} cm at the distance of 1.5 kpc.

for W49B, higher kT_e would be expected in a region with a high ambient gas density if we consider rarefaction as the formation process of RPs.

It is interesting to point out that the plasma in the north-western region is close to CIE with $n_{\text{et}} \sim 10^{12} \text{ s cm}^{-3}$. A possible explanation is that the cooling of the plasma in this region is less efficient since the region is far away from the molecular cloud, which would be the major cooling source for IC 443. Lower ambient gas density, which is suggested by the large shell radius in the west (Lee et al. 2008), would also make the cooling less efficient.

5. CONCLUSIONS

We have performed spatially resolved spectroscopy of X-ray emission from IC 443 with *Suzaku*. Spectra extracted from each region of the remnant are all fitted well with a model consisting of CIE and two RP components. The X-ray absorption column densities are high in regions where the $^{12}\text{CO}(J=1-0)$ emission is bright, indicating that the molecular cloud is located in front of the remnant. The metal abundances of the CIE component as well as its spatial distribution suggest that it is emitted by the shocked ISM. The electron temperature of one of the RP component ranges from 0.16 keV to 0.28 keV whereas that of the other RP compo-

ment is in the range of 0.48–0.67 keV. The electron temperatures of both RP components decrease toward the southeast, where the remnant is interacting with the molecular cloud. Also, the normalization ratio of the lower- kT_e RP to higher- kT_e RP components increases toward the southeast. The two findings may be a result of cooling of the X-ray emitting plasma by the interacting molecular cloud via thermal conduction. The thermal conduction can explain the RP if the cooling proceeds fast enough compared to the recombination timescale of the plasma.

We thank Prof. Katsuji Koyama and Dr. Hiroya Yamaguchi for helpful advice. We are grateful to Dr. Satoshi Yoshiike for providing us with the NANTEN2 data. We deeply appreciate all the *Suzaku* team members. This work is partially supported by JSPS/MEXT Scientific Research Grant Numbers JP15J01842 (H.M.), JP25109004 (T.T. and T.G.T.), JP26800102 (H.U.), JP15H02090 (T.G.T.), and JP26610047 (T.G.T.).

REFERENCES

- Bocchino, F., & Bykov, A. M. 2001, *A&A*, 376, 248
 Bocchino, F., & Bykov, A. M. 2003, *A&A*, 400, 203
 Bocchino, F., Miceli, M., & Troja, E. 2009, *A&A*, 498, 139
 Cornett, R. H., Chin, G., & Knapp, G. R. 1977, *A&A*, 54, 889
 Denoyer, L. K. 1979, *ApJL*, 232, L165
 Dickey, J. M., & Lockman, F. J. 1990, *ARA&A*, 28, 215
 Fesen, R. A., & Kirshner, R. P. 1980, *ApJ*, 242, 1023
 Ishisaki, Y., Maeda, Y., Fujimoto, R., et al. 2007, *PASJ*, 59, 113
 Itoh, H., & Masai, K. 1989, *MNRAS*, 236, 885
 Kawasaki, M. T., Ozaki, M., Nagase, F., et al. 2002, *ApJ*, 572, 897
 Kokusho, T., Nagayama, T., Kaneda, H., et al. 2013, *ApJL*, 768, L8
 Koyama, K., Tsunemi, H., Dotani, T., et al. 2007, *PASJ*, 59, 23
 Lee, J.-J., Koo, B.-C., Yun, M. S., et al. 2008, *AJ*, 135, 796
 Lopez, L. A., Pearson, S., Ramirez-Ruiz, E., et al. 2013, *ApJ*, 777, 145
 Masai, K. 1994, *ApJ*, 437, 770
 Masui, K., Mitsuda, K., Yamasaki, N. Y., et al. 2009, *PASJ*, 61, S115
 Matsumura, H., Uchida, H., Tanaka, T., et al. 2017, *PASJ*, 69, 30
 Morrison, R., & McCammon, D. 1983, *ApJ*, 270, 119
 Olbert, C. M., Clearfield, C. R., Williams, N. E., Keohane, J. W., & Frail, D. A. 2001, *ApJL*, 554, L205
 Ohnishi, T., Uchida, H., Tsuru, T. G., & Koyama, K., 2014, *ApJ*, 784, 74
 Ozawa, M., Koyama, K., Yamaguchi, H., Masai, K., & Tamagawa, T. 2009, *ApJL*, 706, L71
 Petre, R., Szymkowiak, A. E., Seward, F. D., & Willingale, R. 1988, *ApJ*, 335, 215
 Rho, J., & Petre, R. 1998, *ApJL*, 503, L167
 Serlemitsos, P. J., Soong, Y., Chan, K.-W., et al. 2007, *PASJ*, 59, S9
 Tawa, N., Hayashida, K., Nagai, M., et al. 2008, *PASJ*, 60, S11
 Troja, E., Bocchino, F., & Reale, F. et al. 2006, *ApJ*, 649, 258
 Uchida, H., Koyama, K., & Yamaguchi, H. 2015, *ApJ*, 808, 77
 Welsh, B. Y., & Sallmen, S. 2003, *A&A*, 408, 545
 Wilms, J., Allen, A., & McCray, R. 2000, *ApJ*, 542, 914
 Xu, J.-L., Wang, J.-J., & Miller, M. 2011, *ApJ*, 727, 81
 Yamaguchi, H., Ozawa, M., Koyama, K., et al. 2009, *ApJL*, 705, L6
 Yamaguchi, H., Koyama, K., & Uchida, H. 2011, *PASJ*, 63, S837
 Yoshiike, S., 2017, Ph.D. Thesis, Nagoya University

APPENDIX

A. FITTING RESULTS OF THE SPECTRA OF THE REGIONS A AND B

Figure 8 shows spectra of the PWN 1SAX J0617.1+2221 in region A and the point source U061530.75+224910.6 in region B in the 1.6-10.0 keV band after NXB subtraction. We fitted the spectra with a model consisting of a power law and an RP component for the sources and the SNR plasma, respectively. The X-ray absorption was fixed at $7.0 \times 10^{21} \text{ cm}^{-2}$ as determined by Kawasaki et al. (2002). We fixed kT_{init} at 5 keV, whereas kT_e and $n_e t$ were allowed to vary. The abundances of Si and S were allowed to vary, whereas those of Ar and Ca were linked to S. The abundances of the other elements were fixed to solar. The spectra can be reproduced well by the model (Table 4). The photon indices of PWN 1SAX J0617.1+2221 and U061530.75+224910.6 are $1.89^{+0.08}_{-0.07}$ and $2.22^{+0.15}_{-0.16}$, respectively, which we used in the SNR emission analysis (see subsection 3.3). The photon indices and the fluxes of the power-law components are consistent with the results by Bocchino & Bykov (2003), who analyzed *XMM-Newton* data.

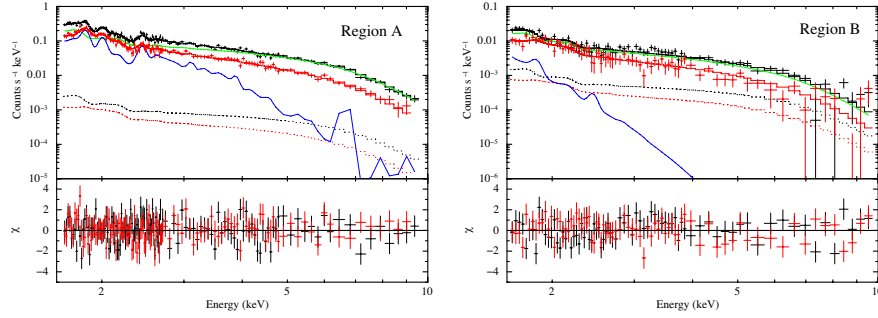


Figure 8. Same as Figure 3 but for regions A and B.

Table 4. Best-fit model parameters of the spectra in regions A and B.

Model function	Parameter	1SAX J0617.1+2221 U061530.75+224910.6	
		region A	region B
TBabs	$N_{\text{H}} (10^{22} \text{ cm}^{-2})$	0.7 (fixed)	0.7 (fixed)
Power law	Photon index	$1.89^{+0.08}_{-0.07}$	$2.22^{+0.15}_{-0.16}$
	Normalization*	801^{+114}_{-94}	254^{+30}_{-50}
VVRNEI	kT_e (keV)	$0.34^{+0.05}_{-0.04}$	$0.31^{+0.49}_{-0.20}$
(RP comp.)	kT_{init} (keV)	5 (fixed)	5 (fixed)
	Z_{Si} (solar)	$2.4^{+0.7}_{-0.5}$	1 (fixed)
	$Z_{\text{S}} = Z_{\text{Ar}} = Z_{\text{Ca}}$ (solar)	$1.3^{+0.4}_{-0.3}$	1 (fixed)
	$n_e t (10^{11} \text{ s cm}^{-3})$	$4.2^{+0.6}_{-0.4}$	> 100
	$VEM (10^{57} \text{ cm}^{-3})^{\dagger}$	$1.2^{+0.2}_{-0.4}$	$1.0^{+5.7}_{-1.0}$
	$\chi^2_{\nu} (\nu)$	1.16 (241)	1.05 (149)

NOTE— *The unit is photons $\text{s}^{-1} \text{cm}^{-2} \text{keV}^{-1} \text{sr}^{-1}$ @ 1 keV.

\dagger Volume emission measure at the distance of 1.5 kpc: $VEM = \int n_e n_{\text{H}} dV$, where n_e , n_{H} , and V are the electron and hydrogen densities, and the emitting volume, respectively.

B. FITTING RESULTS OF THE SPECTRA FROM REGIONS 1–20

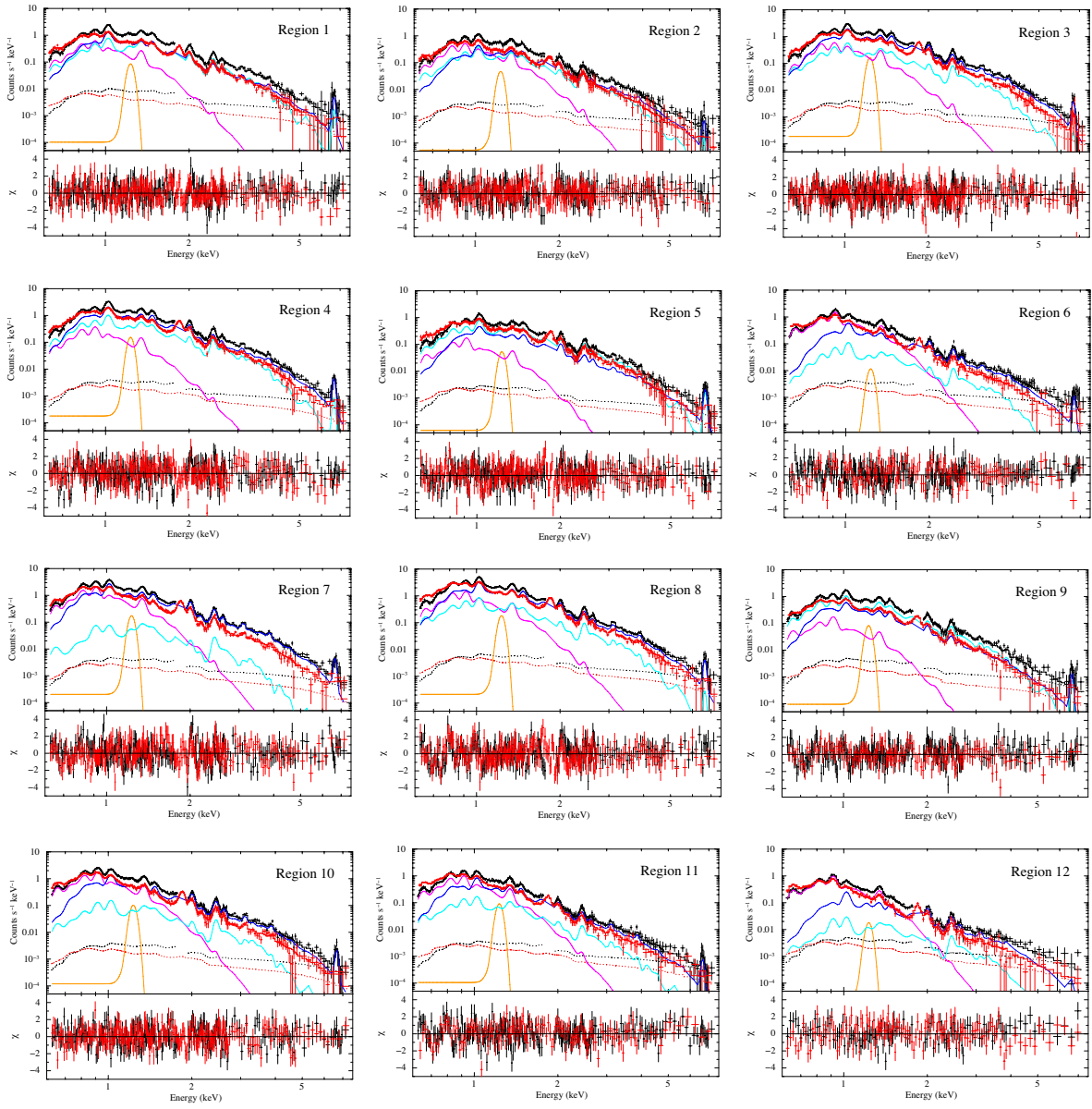


Figure 9. Same as Figure 3 but for regions 1–12.

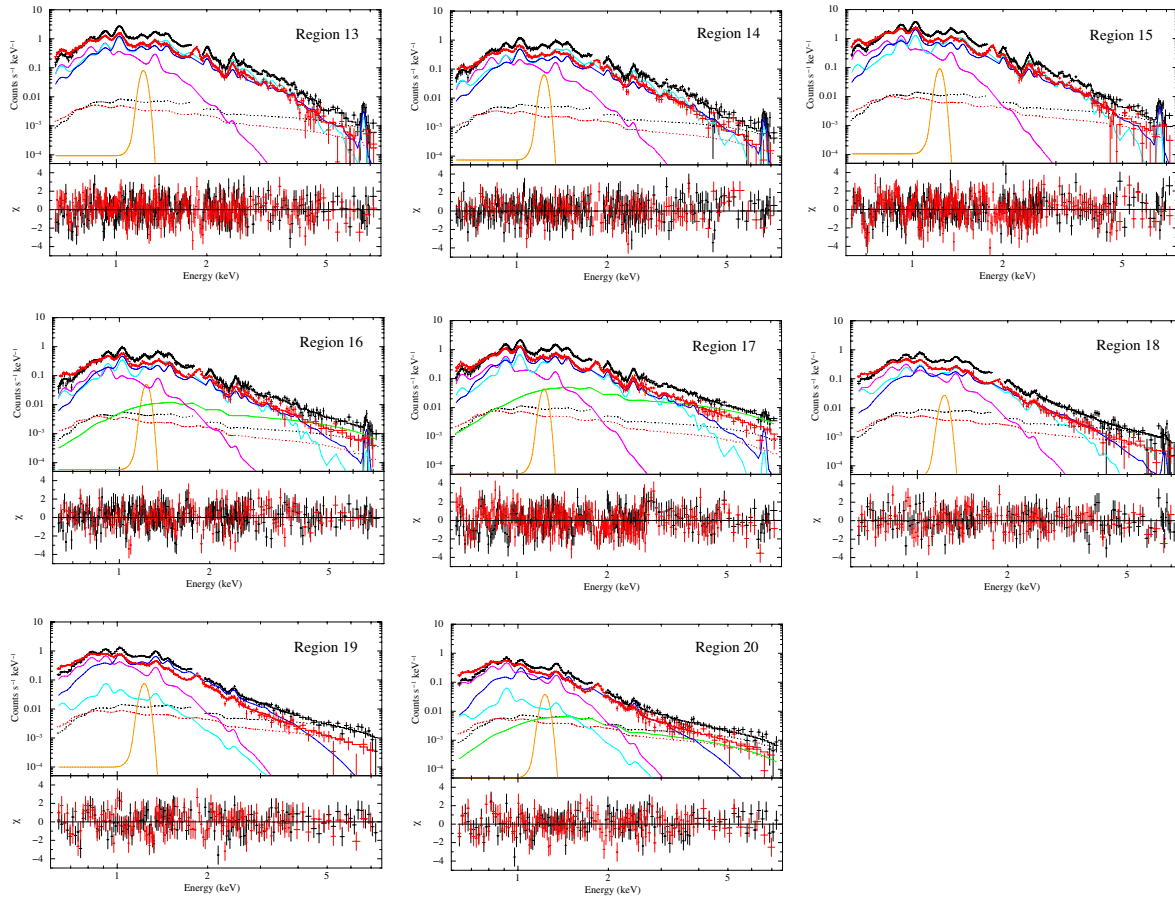


Figure 10. Same as Figure 3 but for regions 13–20.

Table 5. Best-fit model parameters of the spectra from regions 1–10.

Model function	Parameter	reg. 1	reg. 2	reg. 3	reg. 4	reg. 5	reg. 6	reg. 7	reg. 8	reg. 9	reg. 10	
TBabs	N_{H} (10^{22} cm $^{-2}$)	0.94 $^{+0.04}_{-0.04}$	0.95 $^{+0.04}_{-0.04}$	0.82 $^{+0.03}_{-0.04}$	0.79 $^{+0.03}_{-0.03}$	0.88 $^{+0.05}_{-0.06}$	0.89 $^{+0.02}_{-0.02}$	0.79 $^{+0.02}_{-0.02}$	0.70 $^{+0.03}_{-0.02}$	0.84 $^{+0.04}_{-0.05}$	0.74 $^{+0.02}_{-0.03}$	
	kT_e (keV)	0.24 $^{+0.02}_{-0.01}$	0.26 $^{+0.01}_{-0.02}$	0.28 $^{+0.05}_{-0.01}$	0.25 $^{+0.04}_{-0.01}$	0.22 $^{+0.05}_{-0.03}$	0.21 $^{+0.01}_{-0.01}$	0.24 $^{+0.01}_{-0.01}$	0.24 $^{+0.01}_{-0.01}$	0.26 $^{+0.01}_{-0.01}$	0.20 $^{+0.06}_{-0.06}$	0.23 $^{+0.01}_{-0.01}$
VVRNEI1 (CIE comp.)	Z_{aH} (solar)	1 (fixed)										
	VEM (10^{57} cm $^{-3}$) ‡	2.9 $^{+1.3}_{-0.9}$	1.7 $^{+0.6}_{-0.5}$	1.1 $^{+0.5}_{-0.4}$	0.8 $^{+0.4}_{-0.4}$	0.8 $^{+0.7}_{-0.3}$	7.5 $^{+1.1}_{-0.9}$	4.3 $^{+1.7}_{-0.4}$	4.3 $^{+1.7}_{-0.4}$	2.7 $^{+0.6}_{-0.5}$	1.1 $^{+1.1}_{-1.0}$	4.5 $^{+1.0}_{-0.7}$
VVRNEI2 (RP $_{\text{cold}}$ comp.)	kT_e (keV)	0.22 $^{+0.01}_{-0.01}$	0.28 $^{+0.05}_{-0.07}$	0.25 $^{+0.05}_{-0.05}$	0.27 $^{+0.02}_{-0.02}$	0.25 $^{+0.02}_{-0.01}$	0.27 $^{+0.07}_{-0.09}$	0.16 $^{+0.08}_{-0.07}$	0.26 $^{+0.01}_{-0.01}$	0.25 $^{+0.04}_{-0.05}$	0.22 $^{+0.07}_{-0.03}$	
	kT_{init} (keV)	5 (fixed)										
VVRNEI3 (RP $_{\text{hot}}$ comp.)	Z_{Ne} (solar)	2.5 $^{+0.4}_{-0.3}$	1.9 $^{+0.3}_{-0.4}$	2.2 $^{+0.2}_{-0.3}$	1.9 $^{+0.2}_{-0.1}$	2.3 $^{+0.3}_{-0.3}$	5.1 $^{+1.7}_{-1.5}$	2.2 $^{+0.3}_{-0.2}$	1.8 $^{+0.1}_{-0.1}$	2.0 $^{+0.2}_{-0.3}$	3.4 $^{+0.5}_{-0.5}$	
	Z_{Mg} (solar)	1.5 $^{+0.1}_{-0.2}$	1.2 $^{+0.2}_{-0.1}$	1.5 $^{+0.1}_{-0.2}$	1.4 $^{+0.1}_{-0.1}$	1.3 $^{+0.3}_{-0.1}$	2.2 $^{+0.8}_{-0.6}$	1.3 $^{+0.2}_{-0.1}$	1.4 $^{+0.1}_{-0.1}$	1.4 $^{+0.2}_{-0.1}$	1.7 $^{+0.3}_{-0.3}$	
	Z_{Si} (solar)	2.0 $^{+0.2}_{-0.2}$	1.7 $^{+0.2}_{-0.3}$	2.7 $^{+0.2}_{-0.2}$	2.5 $^{+0.2}_{-0.1}$	2.4 $^{+0.2}_{-0.1}$	4.9 $^{+1.6}_{-1.1}$	3.4 $^{+0.1}_{-0.3}$	2.2 $^{+0.1}_{-0.2}$	1.5 $^{+0.2}_{-0.1}$	4.2 $^{+0.6}_{-0.5}$	
	Z_{S} (solar)	1.2 $^{+0.1}_{-0.2}$	1.0 $^{+0.2}_{-0.2}$	1.7 $^{+0.2}_{-0.1}$	1.6 $^{+0.2}_{-0.1}$	1.4 $^{+0.2}_{-0.1}$	3.6 $^{+0.9}_{-0.9}$	2.4 $^{+0.3}_{-0.2}$	1.6 $^{+0.1}_{-0.2}$	0.9 $^{+0.1}_{-0.1}$	3.3 $^{+0.4}_{-0.4}$	
	$Z_{\text{Ar}} = Z_{\text{Ca}}$ (solar)	1.3 $^{+0.3}_{-0.2}$	0.9 $^{+0.5}_{-0.4}$	1.6 $^{+0.3}_{-0.2}$	1.4 $^{+0.2}_{-0.3}$	1.3 $^{+0.3}_{-0.3}$	2.4 $^{+1.2}_{-1.2}$	2.5 $^{+0.4}_{-0.4}$	1.9 $^{+0.3}_{-0.2}$	1.0 $^{+0.2}_{-0.2}$	3.1 $^{+0.8}_{-0.6}$	
	$Z_{\text{Fe}} = Z_{\text{Ni}}$ (solar)	0.7 $^{+0.1}_{-0.1}$	0.4 $^{+0.1}_{-0.1}$	0.5 $^{+0.1}_{-0.1}$	0.5 $^{+0.1}_{-0.1}$	0.8 $^{+0.1}_{-0.1}$	1.1 $^{+0.5}_{-0.3}$	0.6 $^{+0.1}_{-0.1}$	0.5 $^{+0.1}_{-0.1}$	0.8 $^{+0.1}_{-0.1}$	0.8 $^{+0.2}_{-0.1}$	
	n_{eI} (10^{11} s cm $^{-3}$)	4.1 $^{+0.3}_{-0.2}$	5.6 $^{+0.6}_{-0.6}$	5.4 $^{+0.4}_{-0.2}$	5.1 $^{+0.2}_{-0.2}$	4.4 $^{+0.2}_{-0.3}$	5.6 $^{+0.5}_{-0.4}$	5.4 $^{+0.1}_{-0.3}$	5.7 $^{+0.2}_{-0.2}$	5.4 $^{+0.4}_{-0.3}$	5.6 $^{+0.2}_{-0.3}$	
	VEM (10^{57} cm $^{-3}$) ‡	3.3 $^{+0.5}_{-0.5}$	1.1 $^{+0.7}_{-0.5}$	1.2 $^{+0.4}_{-0.3}$	1.8 $^{+0.3}_{-0.4}$	2.1 $^{+0.3}_{-0.3}$	0.1 $^{+0.1}_{-0.1}$	0.1 $^{+0.1}_{-0.1}$	0.3 $^{+0.2}_{-0.2}$	1.8 $^{+0.6}_{-0.5}$	3.2 $^{+0.5}_{-0.5}$	0.3 $^{+0.1}_{-0.1}$
	kT_e (keV)	0.56 $^{+0.04}_{-0.05}$	0.62 $^{+0.07}_{-0.07}$	0.62 $^{+0.02}_{-0.03}$	0.59 $^{+0.03}_{-0.02}$	0.67 $^{+0.06}_{-0.05}$	0.64 $^{+0.06}_{-0.04}$	0.64 $^{+0.06}_{-0.04}$	0.55 $^{+0.03}_{-0.02}$	0.57 $^{+0.02}_{-0.01}$	0.61 $^{+0.04}_{-0.06}$	0.61 $^{+0.03}_{-0.03}$
	kT_{init} (keV)	5 (fixed)										
Gaussian	Z_{aH} (solar)	= RP $_{\text{cold}}$										
	n_{eI} (10^{11} s cm $^{-3}$)	= RP $_{\text{cold}}$										
Power law	VEM (10^{57} cm $^{-3}$) ‡	1.4 $^{+0.2}_{-0.3}$	0.5 $^{+0.3}_{-0.2}$	1.4 $^{+0.2}_{-0.2}$	1.4 $^{+0.2}_{-0.2}$	0.4 $^{+0.1}_{-0.1}$	0.3 $^{+0.1}_{-0.1}$	1.5 $^{+0.2}_{-0.1}$	2.2 $^{+0.2}_{-0.2}$	0.6 $^{+0.1}_{-0.1}$	0.6 $^{+0.1}_{-0.1}$	
	Centroid (keV)	1.23 (fixed)										
Photon index	Normalization ‡	14 $^{+7}_{-7}$	19 $^{+11}_{-11}$	47 $^{+10}_{-13}$	46 $^{+13}_{-12}$	24 $^{+13}_{-6}$	3 $^{+9}_{-3}$	42 $^{+11}_{-12}$	30 $^{+8}_{-8}$	22 $^{+8}_{-8}$	30 $^{+10}_{-12}$	
	Photon index	—	—	—	—	—	—	—	—	—	—	
Normalization*	χ^2_{ν} (ν)	1.13 (477)	1.15 (477)	1.12 (485)	1.32 (477)	1.17 (477)	1.24 (365)	1.39 (477)	1.30 (477)	1.04 (365)	1.16 (477)	
		—	—	—	—	—	—	—	—	—	—	

NOTE— ‡ Volume emission measure at the distance of 1.5 kpc: $VEM = \int n_e n_{\text{H}} dV$, where n_e , n_{H} , and V are the electron and hydrogen densities, and the emitting volume, respectively. ‡ The unit is photons s $^{-1}$ cm $^{-2}$ sr $^{-1}$.*The unit is photons s $^{-1}$ cm $^{-2}$ keV $^{-1}$ sr $^{-1}$ at 1 keV.

Table 6. Best-fit model parameters of the spectra from regions 11–20.

Model function	Parameter	reg. 11	reg. 12	reg. 13	reg. 14	reg. 15	reg. 16	reg. 17	reg. 18	reg. 19	reg. 20
TBabs	N_{H} (10^{22} cm $^{-2}$)	0.74 $^{+0.04}_{-0.03}$	0.81 $^{+0.02}_{-0.03}$	0.88 $^{+0.03}_{-0.03}$	0.98 $^{+0.04}_{-0.05}$	0.77 $^{+0.03}_{-0.03}$	0.91 $^{+0.14}_{-0.09}$	0.96 $^{+0.03}_{-0.03}$	0.85 $^{+0.04}_{-0.03}$	0.67 $^{+0.02}_{-0.03}$	0.77 $^{+0.05}_{-0.02}$
	kT_e (keV)	0.24 $^{+0.01}_{-0.01}$	0.22 $^{+0.01}_{-0.01}$	0.24 $^{+0.02}_{-0.02}$	0.27 $^{+0.02}_{-0.03}$	0.20 $^{+0.02}_{-0.01}$	0.24 $^{+0.05}_{-0.05}$	0.19 $^{+0.01}_{-0.01}$	0.25 $^{+0.05}_{-0.06}$	0.27 $^{+0.01}_{-0.01}$	0.24 $^{+0.01}_{-0.01}$
(CIE comp.)	Z_{aH} (solar)	1 (fixed)									
	VEM (10^{57} cm $^{-3}$) ‡	2.7 $^{+0.8}_{-0.4}$	4.5 $^{+0.6}_{-0.7}$	2.1 $^{+0.6}_{-0.5}$	0.9 $^{+0.3}_{-0.3}$	5.5 $^{+1.5}_{-1.5}$	0.7 $^{+2.0}_{-0.4}$	5.3 $^{+1.3}_{-0.7}$	1.0 $^{+0.3}_{-0.4}$	1.3 $^{+0.2}_{-0.2}$	1.7 $^{+0.8}_{-0.6}$
VVRNEI	kT_e (keV)	0.24 $^{+0.05}_{-0.07}$	0.26 $^{+0.09}_{-0.08}$	0.21 $^{+0.02}_{-0.11}$	0.19 $^{+0.02}_{-0.01}$	0.18 $^{+0.01}_{-0.01}$	0.19 $^{+0.01}_{-0.02}$	0.19 $^{+0.04}_{-0.03}$	0.22 $^{+0.02}_{-0.02}$	0.24 $^{+0.04}_{-0.05}$	0.22 $^{+0.09}_{-0.08}$
	kT_{int} (keV)	5 (fixed)									
(RP $_{\text{cold}}$ comp.)	Z_{Ne} (solar)	2.0 $^{+0.3}_{-0.3}$	6.8 $^{+5.4}_{-2.9}$	2.3 $^{+0.3}_{-0.4}$	2.4 $^{+0.5}_{-0.4}$	4.4 $^{+0.7}_{-0.6}$	3.9 $^{+2.0}_{-0.9}$	5.0 $^{+0.4}_{-0.5}$	1.9 $^{+0.3}_{-0.3}$	1.5 $^{+0.1}_{-0.2}$	2.6 $^{+1.1}_{-0.7}$
	Z_{Mg} (solar)	1.5 $^{+0.3}_{-0.2}$	2.9 $^{+4.1}_{-1.3}$	1.3 $^{+0.1}_{-0.3}$	1.4 $^{+0.3}_{-0.3}$	1.9 $^{+0.3}_{-0.1}$	2.0 $^{+0.8}_{-0.5}$	2.4 $^{+0.2}_{-0.2}$	1.1 $^{+0.1}_{-0.2}$	1.1 $^{+0.1}_{-0.1}$	1.5 $^{+0.4}_{-0.2}$
	Z_{Si} (solar)	1.7 $^{+0.4}_{-0.2}$	9.5 $^{+5.3}_{-3.5}$	1.6 $^{+0.1}_{-0.2}$	1.2 $^{+0.2}_{-0.2}$	2.3 $^{+0.3}_{-0.2}$	1.9 $^{+0.6}_{-0.3}$	2.5 $^{+0.2}_{-0.2}$	0.7 $^{+0.1}_{-0.2}$	0.7 $^{+0.1}_{-0.2}$	1.4 $^{+0.4}_{-0.2}$
	Z_{S} (solar)	1.1 $^{+0.2}_{-0.2}$	6.7 $^{+4.3}_{-2.5}$	0.9 $^{+0.1}_{-0.1}$	0.8 $^{+0.1}_{-0.1}$	1.4 $^{+0.1}_{-0.2}$	1.1 $^{+0.4}_{-0.2}$	1.1 $^{+0.2}_{-0.2}$	1.8 $^{+0.2}_{-0.2}$	0.3 $^{+0.1}_{-0.1}$	0.8 $^{+0.3}_{-0.2}$
	$Z_{\text{Ar}} = Z_{\text{Ca}}$ (solar)	1.8 $^{+0.6}_{-0.5}$	5.2 $^{+5.4}_{-3.1}$	0.8 $^{+0.2}_{-0.2}$	0.8 $^{+0.2}_{-0.2}$	1.4 $^{+0.3}_{-0.2}$	1.2 $^{+0.6}_{-0.5}$	2.0 $^{+0.5}_{-0.5}$	2.0 $^{+0.5}_{-0.5}$	$= Z_{\text{S}}$	$= Z_{\text{S}}$
	$Z_{\text{Fe}} = Z_{\text{Ni}}$ (solar)	0.5 $^{+0.2}_{-0.1}$	0.8 $^{+1.2}_{-0.5}$	0.3 $^{+0.1}_{-0.1}$	0.4 $^{+0.2}_{-0.2}$	0.8 $^{+0.2}_{-0.2}$	0.7 $^{+0.5}_{-0.2}$	0.6 $^{+0.1}_{-0.2}$	0.3 $^{+0.1}_{-0.1}$	0.2 $^{+0.1}_{-0.1}$	0.4 $^{+0.1}_{-0.1}$
	n_{eI} (10^{11} s cm $^{-3}$)	5.8 $^{+0.5}_{-0.4}$	5.7 $^{+0.7}_{-0.5}$	3.8 $^{+0.3}_{-0.3}$	3.8 $^{+0.4}_{-0.4}$	4.3 $^{+0.2}_{-0.1}$	4.7 $^{+0.4}_{-0.5}$	4.8 $^{+0.2}_{-0.2}$	5.8 $^{+0.7}_{-0.7}$	12.3 $^{+2.3}_{-1.7}$	15.1 $^{+8.3}_{-4.1}$
	VEM (10^{57} cm $^{-3}$) ‡	0.5 $^{+0.4}_{-0.4}$	≤ 0.1	3.7 $^{+0.5}_{-0.4}$	2.3 $^{+0.5}_{-0.5}$	3.2 $^{+0.6}_{-0.5}$	1.1 $^{+0.3}_{-0.4}$	1.1 $^{+0.3}_{-0.4}$	1.7 $^{+0.6}_{-0.8}$	1.5 $^{+0.6}_{-0.4}$	≤ 0.2
	kT_e (keV)	0.54 $^{+0.03}_{-0.08}$	0.63 $^{+0.10}_{-0.08}$	0.48 $^{+0.07}_{-0.19}$	0.59 $^{+0.07}_{-0.14}$	0.54 $^{+0.04}_{-0.03}$	0.64 $^{+0.06}_{-0.11}$	0.64 $^{+0.06}_{-0.11}$	0.55 $^{+0.04}_{-0.04}$	0.63 $^{+0.07}_{-0.04}$	0.62 $^{+0.02}_{-0.01}$
	kT_{int} (keV)	5 (fixed)									
(RP $_{\text{hot}}$ comp.)	Z_{aH} (solar)	$= \text{RP}_{\text{cold}}$									
	n_{eI} (10^{11} s cm $^{-3}$)	$= \text{RP}_{\text{cold}}$									
Gaussian	VEM (10^{57} cm $^{-3}$) ‡	0.5 $^{+0.3}_{-0.2}$	0.1 $^{+0.1}_{-0.1}$	1.2 $^{+1.1}_{-1.0}$	0.5 $^{+0.4}_{-0.1}$	0.9 $^{+0.2}_{-0.1}$	0.3 $^{+0.1}_{-0.1}$	0.7 $^{+0.2}_{-0.1}$	0.3 $^{+0.1}_{-0.1}$	0.8 $^{+0.1}_{-0.1}$	0.3 $^{+0.1}_{-0.1}$
	Centroid (keV)	1.23 (fixed)									
Power law	Normalization ‡	28 $^{+8}_{-8}$	5 $^{+4}_{-5}$	12 $^{+7}_{-7}$	15 $^{+8}_{-4}$	9 $^{+5}_{-5}$	11 $^{+7}_{-8}$	4 $^{+4}_{-4}$	4 $^{+3}_{-2}$	5 $^{+1}_{-1}$	6 $^{+2}_{-2}$
	Photon index	—	—	—	—	—	1.89 (fixed)	1.89 (fixed)	—	—	2.22 (fixed)
Normalization*	—	—	—	—	—	—	45 $^{+9}_{-9}$	97 $^{+7}_{-7}$	—	—	18 $^{+4}_{-5}$
	χ^2_{ν} (ν)	1.18 (365)	1.35 (250)	1.25 (477)	1.22 (365)	1.53 (477)	1.13 (364)	1.36 (476)	1.19 (273)	1.27 (257)	1.18 (256)

NOTE— ‡ Volume emission measure at the distance of 1.5 kpc: $VEM = \int n_e n_{\text{H}} dV$, where n_e , n_{H} , and V are the electron and hydrogen densities, and the emitting volume, respectively. ‡ The unit is photons s $^{-1}$ cm $^{-2}$ sr $^{-1}$.*The unit is photons s $^{-1}$ cm $^{-2}$ keV $^{-1}$ sr $^{-1}$ at 1 keV.